

Magnetic Properties

Single-Molecule Magnets $\text{DyM}_2\text{N@C}_{80}$ and $\text{Dy}_2\text{MN@C}_{80}$ ($M = \text{Sc}, \text{Lu}$): The Impact of Diamagnetic Metals on Dy^{3+} Magnetic Anisotropy, Dy...Dy Coupling, and Mixing of Molecular and Lattice VibrationsLukas Spree,^[a] Christin Schlesier,^[a] Aram Kostanyan,^[b] Rasmus Westerström,^[b, c] Thomas Greber,^[b] Bernd Büchner,^[a] Stanislav M. Avdoshenko,^{*,[a]} and Alexey A. Popov^{*,[a]}

Abstract: The substitution of scandium in fullerene single-molecule magnets (SMMs) $\text{DySc}_2\text{N@C}_{80}$ and $\text{Dy}_2\text{ScN@C}_{80}$ by lutetium has been studied to explore the influence of the diamagnetic metal on the SMM performance of dysprosium nitride clusterfullerenes. The use of lutetium led to an improved SMM performance of $\text{DyLu}_2\text{N@C}_{80}$, which shows a higher blocking temperature of magnetization ($T_B = 9.5$ K), longer relaxation times, and broader hysteresis than $\text{DySc}_2\text{N@C}_{80}$ ($T_B = 6.9$ K). At the same time, $\text{Dy}_2\text{LuN@C}_{80}$ was found to have a similar blocking temperature of magnetization to $\text{Dy}_2\text{ScN@C}_{80}$ ($T_B = 8$ K), but substantially different in-

teractions between the magnetic moments of the dysprosium ions in the Dy_2MN clusters. Surprisingly, although the intramolecular dipolar interactions in $\text{Dy}_2\text{LuN@C}_{80}$ and $\text{Dy}_2\text{ScN@C}_{80}$ are of similar strength, the exchange interactions in $\text{Dy}_2\text{LuN@C}_{80}$ are close to zero. Analysis of the low-frequency molecular and lattice vibrations showed strong mixing of the lattice modes and endohedral cluster vibrations in k -space. This mixing simplifies the spin–lattice relaxation by conserving the momentum during the spin flip and helping to distribute the moment and energy further into the lattice.

Introduction

Enclosing lanthanide ions within the fullerene cage is a versatile route to a variety of molecular magnets.^[1] In particular, when non-metal atoms (C, N, O, S) are captured by the carbon cage together with lanthanides, the strong ionic interactions emerging in such endohedral clusterfullerenes may lead to a large magnetic anisotropy.^[2] In addition, different magnetic states can emerge from the intramolecular interactions of lanthanide ions in clusterfullerenes.^[2a,e,3] This combination of properties made lanthanide-clusterfullerenes promising candidates for single-molecule magnets (SMMs). Single-molecule

magnetism is a phenomenon involving the slow relaxation of magnetization in molecules with a bistable magnetic ground state and has been a hot topic in the field of molecular magnetism during the last decades.^[4] Indeed, some lanthanide-clusterfullerenes exhibit single-molecule magnetism,^[5] which is most robust in dysprosium-clusterfullerenes.^[1c,2d-f,3a,6]

Nitride clusterfullerenes (NCFs) with the composition $(\text{M}^{3+})_3\text{N}^{3-}\text{@C}_{2n}^{6-}$, and in particular the species with $\text{C}_{2n} = \text{C}_{80}\text{-}I_h$ (I_h denotes the symmetry of the carbon cage) and $M = \text{Sc}, \text{Y}$, or heavy lanthanides (Gd–Lu), show the largest synthetic yield and are therefore the most studied clusterfullerenes to date.^[1a,b,7] The structure of the trimetal nitride cluster, with N^{3-} in its center and three M^{3+} ions located at the vertices of the triangle with rather short M–N bonds, offers a convenient platform to create a variety of molecular magnets with divergent properties. First of all, the nitride ion at a distance of only 2.0–2.2 Å from the lanthanide^[2d,6b,8] generates a strong axial ligand field (LF), which leads to an easy-axis magnetic anisotropy for cerium, praseodymium, neodymium, terbium, dysprosium, and holmium ions, and an easy-plane anisotropy for erbium and thulium ions^[2b] (note that we use the term “ligand field” instead of the more commonly used “crystal field” to avoid unnecessary connotations to intermolecular interactions in crystals). The strong axial LF also ensures that m_J is a good quantum number, at least for several lowest-energy LF states. In particular, the lowest-energy Kramers doublets for Dy^{3+} in dysprosium-scandium NCFs are essentially pure m_J states, with the high-spin $J_z = \pm 15/2$ states as the ground Kramers doublet with the magnetic moment oriented along the Dy–N bond.^[2a,c]

[a] L. Spree, C. Schlesier, Prof. Dr. B. Büchner, Dr. S. M. Avdoshenko, Dr. A. A. Popov
Leibniz Institute for Solid State and Materials Research (IFW Dresden)
01069 Dresden (Germany)
E-mail: s.adoshenk@ifw-dresden.de
a.popov@ifw-dresden.de

[b] Dr. A. Kostanyan, Dr. R. Westerström, Prof. Dr. T. Greber
Physik-Institut der Universität Zürich
Winterthurerstr. 190, 8057 Zürich (Switzerland)

[c] Dr. R. Westerström
The Division of Synchrotron Radiation Research
Lund University, 22100 Lund (Sweden)

Supporting information and the ORCID identification number(s) for the author(s) of this article can be found under:
<https://doi.org/10.1002/chem.201904879>.

© 2019 The Authors. Published by Wiley-VCH Verlag GmbH & Co. KGaA. This is an open access article under the terms of the Creative Commons Attribution License, which permits use, distribution and reproduction in any medium, provided the original work is properly cited.

The purity of the J_z states in terms of m_j composition ensures that the magnetic system is weakly susceptible to external perturbations such as those introduced by dipolar magnetic fields from neighboring molecules or molecular and lattice vibrations.

Another advantage that lanthanide NCFs offer for tuning magnetic properties is the possibility of combining different metals within one molecule to give the so-called mixed-metal NCFs.^[5a,8c,9] The importance of this can be best illustrated with the dysprosium-scandium NCFs $\text{Dy}_x\text{Sc}_{3-x}\text{N}@C_{80}\text{-I}_h$ ($x=1-3$) as an example.^[3a] As Sc^{3+} is diamagnetic, this series essentially allows analysis of how two or three dysprosium ions interact magnetically and the effect of these interactions on SMM behavior. $\text{DySc}_2\text{N}@C_{80}\text{-I}_h$ was the first endohedral metallofullerene (EMF) proven to be a SMM.^[6b,d] At temperatures below 7 K, the molecule exhibits magnetic hysteresis with the abrupt drop of the magnetization in zero magnetic field ascribed to the quantum tunneling of magnetization (QTM), which is typical for single-ion magnets. $\text{Dy}_2\text{ScN}@C_{80}\text{-I}_h$ shows magnetic hysteresis below 8 K without fast QTM relaxation in zero field, which is explained by ferromagnetic exchange and dipolar coupling between the non-collinear magnetic moments of the two dysprosium ions in the Dy_2ScN cluster (Figure 1), thus creating an ad-

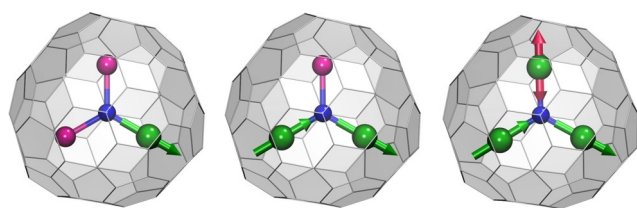


Figure 1. Molecular structures of $\text{Dy}_x\text{M}_{3-x}\text{N}@C_{80}\text{-I}_h$ nitride clusterfullerenes ($\text{M}=\text{Sc}$ or Lu ; $x=1-3$) and schematic illustration of the coupling of magnetic moments. Dy is green, M is magenta, N is blue, C is light gray. The magnetic moments of Dy ions are visualized as green or red arrows. In $\text{DyM}_2\text{N}@C_{80}$ (left), the magnetic moment is aligned along the Dy–N bond. In the magnetic ground state of $\text{Dy}_2\text{MN}@C_{80}$ (middle), the magnetic moments of the two Dy ions are coupled ferromagnetically. In $\text{Dy}_3\text{N}@C_{80}$ (right), the ground magnetic state is frustrated, and the magnetic moment of the Dy ion illustrated with a red arrow can switch between two isoenergetic orientations without changing the orientation of the two other moments.

ditional barrier and preventing zero-field QTM.^[3a] The temperature dependence of the magnetization relaxation times in $\text{Dy}_2\text{ScN}@C_{80}\text{-I}_h$ revealed a high barrier of 1735 K, because of the Orbach relaxation via the fifth Kramers doublet, in good agreement with CASSCF calculations.^[2d] Similar ferromagnetic interactions between dysprosium ions are also present in $\text{Dy}_3\text{N}@C_{80}\text{-I}_h$, but the triangular arrangement of the dysprosium ions forbids simultaneous realization of ferromagnetic coupling for all three Dy...Dy contacts resulting in a frustrated ground state (Figure 1) with faster relaxation of magnetization than in the mono- and dinuclear analogues.^[2a,3a] Thus, due to different cluster compositions and intramolecular Dy...Dy interactions, $\text{DySc}_2\text{N}@C_{80}\text{-I}_h$, $\text{Dy}_2\text{ScN}@C_{80}\text{-I}_h$, and $\text{Dy}_3\text{N}@C_{80}\text{-I}_h$ exhibit substantially different SMM behavior at low temperatures.

It is natural to consider that the magnetic properties of the NCFs in the $\text{Dy}_x\text{Sc}_{3-x}\text{N}@C_{80}\text{-I}_h$ ($x=1-3$) series discussed above

are determined by the Dy^{3+} ions, with the diamagnetic Sc^{3+} ions acting just as placeholders, which are needed to keep the trimetallic cluster composition. However, in this work, we shed more light on the role that the diamagnetic metal can play in the SMM properties of NCFs. For this, we chose lutetium as a diamagnetic lanthanide, the ionic radius ($R^{3+}=0.86$ Å) of which is noticeably larger than that of scandium ($R^{3+}=0.75$ Å). Yet, as we reported recently, $\text{DyLu}_2\text{N}@C_{80}\text{-I}_h$ and $\text{Dy}_2\text{LuN}@C_{80}\text{-I}_h$ can still be synthesized, albeit in lower yields than the dysprosium-scandium analogues.^[8c] The larger size of Lu^{3+} leads to changes in the internal structure of the trimetallic nitride cluster, and in particular results in shorter Dy–N bonds than in the dysprosium-scandium NCFs. The shortening of the Dy–N bonds may affect the magnetic anisotropy and the strength of the intramolecular Dy...Dy coupling. Furthermore, lutetium is much heavier than scandium, which changes the low-frequency part of the vibrational spectrum. Because the relaxation of magnetization involves spin–phonon interactions, alterations of molecular vibrations may also result in changes in the SMM properties. Thus, the goal of this work was to study a possible influence of these factors on the SMM properties of the $\text{DyM}_2\text{N}@C_{80}\text{-I}_h$ and $\text{Dy}_2\text{MN}@C_{80}\text{-I}_h$ NCFs.

Results and Discussion

Magnetization behavior of $\text{DyLu}_2\text{N}@C_{80}$ and $\text{Dy}_2\text{LuN}@C_{80}$

The mixed-metal dysprosium-lutetium NCFs with a $C_{80}\text{-I}_h$ fullerene cage (for clarity, the symmetry designation will be omitted hereafter) were obtained by arc-discharge synthesis and separated by recycling HPLC as reported earlier.^[8c] Similar retention behavior of $\text{Dy}_3\text{N}@C_{80}$, $\text{Dy}_2\text{LuN}@C_{80}$, $\text{DyLu}_2\text{N}@C_{80}$, and $\text{Lu}_3\text{N}@C_{80}$ substantially complicated the separation of the individual compounds. However, a compositional purity exceeding 90–95% could be achieved for $\text{Dy}_2\text{LuN}@C_{80}$, as verified by MS analysis. Due to the very similar retention behavior, the separation of $\text{DyLu}_2\text{N}@C_{80}$ from $\text{Lu}_3\text{N}@C_{80}$ was not possible, and the relative content of the two NCFs in the studied sample was around 1:1.35. Because $\text{Lu}_3\text{N}@C_{80}$ is diamagnetic, its presence in the sample does not lead to strong changes in the magnetic properties of $\text{DyLu}_2\text{N}@C_{80}$. A possible influence of dilution on the quantum tunneling of magnetization will be specifically considered below.

The magnetization curves of $\text{DyLu}_2\text{N}@C_{80}$ and $\text{Dy}_2\text{LuN}@C_{80}$, measured by SQUID (superconducting quantum interference device) magnetometry, are shown in Figures 2 and 3, respectively. $\text{DyLu}_2\text{N}@C_{80}$ exhibits hysteresis up to 9 K at a sweep rate of 3 mT s^{-1} (Figure 2a). The “butterfly” shape of the hysteresis curves points to efficient zero-field relaxation by QTM similar to that observed in $\text{DySc}_2\text{N}@C_{80}$ (Figure 2b).^[6d] However, in the latter, the opening of the hysteresis is narrower and the QTM induces complete loss of magnetization at zero field, whereas in $\text{DyLu}_2\text{N}@C_{80}$, upon crossing zero-field, the magnetization drops to around 30% of the saturation magnetization value, resulting in a coercivity of 0.9 T at 2 K. Recently, we showed that the QTM in $\text{DySc}_2\text{N}@C_{80}$ is strongly affected by dilution in the diamagnetic matrix, including dilution with $\text{Lu}_3\text{N}@C_{80}$.^[6b] To

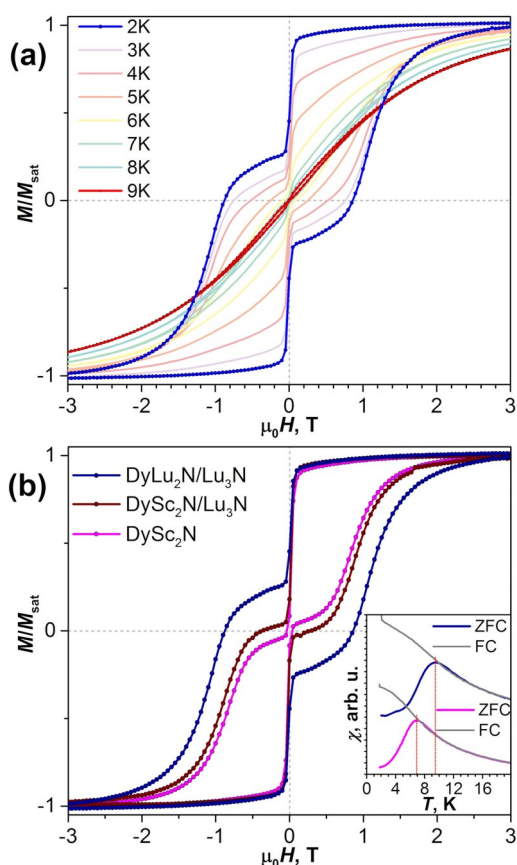


Figure 2. (a) Magnetization curves of the $\text{DyLu}_2\text{N@C}_{80}/\text{Lu}_3\text{N@C}_{80}$ sample measured between 2 and 9 K (average sweep rate 2.9 mT s^{-1}). (b) Magnetization curves of $\text{DyLu}_2\text{N@C}_{80}/\text{Lu}_3\text{N@C}_{80}$ measured at 2 K and compared with those of $\text{DySc}_2\text{N@C}_{80}$ and $\text{DySc}_2\text{N@C}_{80}$ diluted with $\text{Lu}_3\text{N@C}_{80}$ in a 1:1 ratio. The inset in (b) shows the determination of the blocking temperature, T_B , from the temperature dependence of the magnetic susceptibility, χ (temperature sweep rate of 5 K min^{-1}).

ensure that the difference in the QTM is intrinsic for the two NCFs and is not caused by the dilution of $\text{DyLu}_2\text{N@C}_{80}$ with $\text{Lu}_3\text{N@C}_{80}$, in Figure 2b we also show the magnetization curve of $\text{DySc}_2\text{N@C}_{80}$ diluted with $\text{Lu}_3\text{N@C}_{80}$ in a ratio of 1:1. This magnetic dilution indeed reduces the QTM step in $\text{DySc}_2\text{N@C}_{80}$ slightly, but the changes do not reach the magnitude observed for $\text{DyLu}_2\text{N@C}_{80}$. Thus, it can be concluded that the zero-field QTM relaxation of magnetization in $\text{DyLu}_2\text{N@C}_{80}$ is slower than in $\text{DySc}_2\text{N@C}_{80}$. Furthermore, the blocking temperature of magnetization, T_B , defined as the temperature of peak magnetic susceptibility measured at 0.2 T for the sample cooled in zero field, is higher for $\text{DyLu}_2\text{N@C}_{80}$ ($T_B = 9.5 \text{ K}$) than for $\text{DySc}_2\text{N@C}_{80}$ ($T_B = 6.9 \text{ K}$). Note that the magnetic dilution does not affect the T_B value,^[6b] and thus the different SMM properties of $\text{DyLu}_2\text{N@C}_{80}$ and $\text{DySc}_2\text{N@C}_{80}$ cannot be caused by the presence of $\text{Lu}_3\text{N@C}_{80}$ in the former. To conclude, $\text{DyLu}_2\text{N@C}_{80}$ was found to be a stronger SMM than $\text{DySc}_2\text{N@C}_{80}$. The substitution of scandium by lutetium in $\text{DyM}_2\text{N@C}_{80}$ leads to slower QTM relaxation, slower in-field relaxation, and a broader magnetic hysteresis with remanence.

For $\text{Dy}_2\text{MN@C}_{80}$, the influence of the diamagnetic metal on the SMM behavior appears to be weaker than for $\text{DyM}_2\text{N@C}_{80}$.

Similarly to $\text{Dy}_2\text{ScN@C}_{80}$, $\text{Dy}_2\text{LuN@C}_{80}$ exhibits open hysteresis without a pronounced QTM step (Figure 3a). Its blocking temperature of magnetization, $T_B = 8 \text{ K}$, is the same as that of $\text{Dy}_2\text{ScN@C}_{80}$.^[2d] However, at 2 K, the magnetic hysteresis of $\text{Dy}_2\text{LuN@C}_{80}$ is narrower (Figure 3b) and the coercive field of 0.4 T is smaller than that of $\text{Dy}_2\text{ScN@C}_{80}$ (0.7 T). Thus, the substitution of scandium by lutetium narrows the magnetic hysteresis but does not change the temperature scale of the slow relaxation. Nevertheless, as we show below, the temperature dependence of relaxation times reveals that the mechanisms of the relaxation of magnetization in $\text{Dy}_2\text{LuN@C}_{80}$ and $\text{Dy}_2\text{ScN@C}_{80}$ are different.

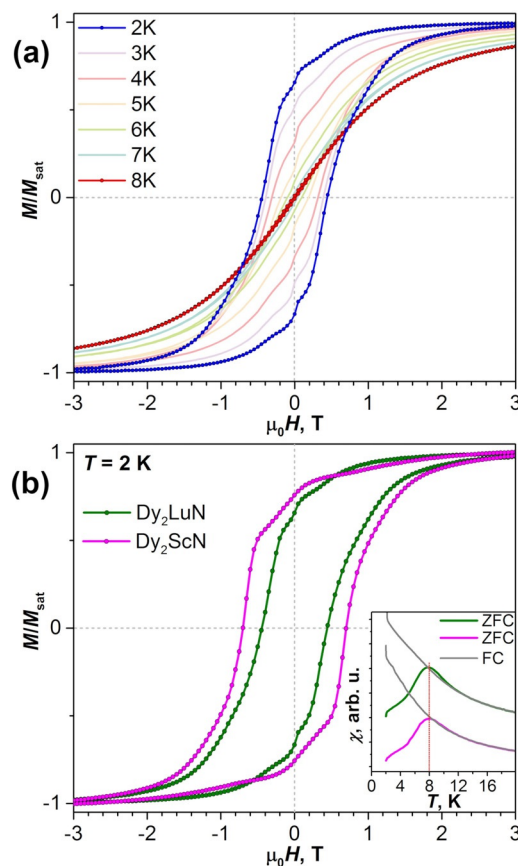


Figure 3. (a) Magnetization curves of the $\text{Dy}_2\text{LuN@C}_{80}$ sample measured between 2 and 8 K (average sweep rate 2.9 mT s^{-1}). (b) Magnetization curve of $\text{Dy}_2\text{LuN@C}_{80}$ measured at 2 K and compared with that of $\text{Dy}_2\text{ScN@C}_{80}$. The inset in (b) shows the determination of the blocking temperature, T_B , from the temperature dependence of the magnetic susceptibility, χ (temperature sweep rate of 5 K min^{-1}).

Relaxation times of magnetization in $\text{DyM}_2\text{N@C}_{80}$ and $\text{Dy}_2\text{MN@C}_{80}$

The opening of magnetic hysteresis in the magnetization curves of molecular magnets indicates that the magnetization attains its equilibrium value slower than the rate of the magnetic field sweep. The slow relaxation of magnetization is a key characteristic of SMMs and needs to be understood in detail. The relaxation of magnetization requires energy exchange between the spin system and a thermal bath, which is mediated

by the phonon system. The spin–phonon interaction is crucial for such an energy exchange, and the role of vibrational degrees of freedom becomes paramount. Several mechanisms of phonon-mediated spin relaxation have been recognized in studies of paramagnetic salts and adapted for SMMs.

A direct mechanism implies a single-phonon process in which phonon frequency matches the energy difference between two opposite spins. Because a magnetic field increases the energy gap between the opposite spins, and the phonon density at near-zero frequency is low and increases with frequency, the relaxation due to a direct mechanism accelerates in a magnetic field according to Equation (1)

$$\tau_{M,dir}^{-1}(H) = A_1 H^4 T + A_2 H^2 T \quad (1)$$

in which τ_M is the magnetization relaxation time, H is the magnetic field, with two terms describing the relaxation of a Kramers ion in the absence (ca. H^4) and in the presence (ca. H^2) of hyperfine interactions, and A_1 and A_2 are fitting parameters. Thus, the relaxation rate scales linearly with temperature, $\tau_{M,dir}^{-1} \sim T$. However, when at low temperature the phonon density may be very low, the energy exchange between the phonon system and the bath can become the limiting step. This effect, known as a phonon bottleneck, can change the temperature dependence to $\tau_{M,dir}^{-1} \sim T^2$.

The Raman mechanism implies a spin flip through the absorption and emission of two phonons, with the frequency difference being equal to the energy gap between the opposite spins. As the frequencies can be much higher than the Zeeman energy, and the phonon density increases with frequency, the Raman mechanism is more efficient than the direct mechanism once the temperature is sufficiently high to ensure sufficient phonon population. The original consideration with only acoustic phonons in the Debye model gave the power-law temperature dependence expressed by Equation (2)

$$\tau_{M,Ram}^{-1}(T) = CT^n \quad (2)$$

in which $n=9$ for Kramers ions and $n=7$ for non-Kramers ions, and C is the fitting parameter.^[10] However, if optical phonons are also included in the model, powers of 6, 5, and even lower can be expected.^[11]

A special case of the Raman mechanism, in which the absorbed phonon energy corresponds to the real excited spin state, is known as the Orbach mechanism. The temperature dependence of the relaxation rate under the Orbach mechanism has an Arrhenius form, expressed by Equation (3)

$$\tau_{M,Orb}^{-1}(T) = \tau_0^{-1} \exp(-U^{eff}/T) \quad (3)$$

in which U^{eff} is the effective barrier (corresponding to the energy of the excited magnetic state) and τ_0 is the attempt time.^[10]

Finally, the QTM is a ubiquitous and characteristic relaxation mechanism of SMMs. In QTM, the spin flips to the opposite direction without energy transfer. As such, it should not show

temperature dependence. The key condition for QTM is the energy matching of the opposite spin levels, and therefore the application of a magnetic field can quench the QTM when Zeeman splitting becomes large enough.

It has become common practice to analyze the relaxation of magnetization in SMMs as a combination of these processes.^[4f,12] Characteristic temperature and field dependencies of relaxation times allow identification of the prevailing relaxation mechanism. Usually, the direct mechanism is the most important at the lowest temperatures of a few K, at somewhat higher temperatures the Raman mechanism becomes dominant, and with further increases in temperature, the Orbach mechanism involving LF excited states takes over. Neither the direct nor Raman mechanism would show an Arrhenius temperature dependence, so the latter usually serves as an indication of the Orbach mechanism. However, back in the 1960s, Klemens^[13] and others^[14] argued that a localized vibrational mode can cause an Arrhenius temperature dependence with U^{eff} corresponding to the frequency of the mode. Furthermore, it was shown that the direct mechanism can also demonstrate Arrhenius behavior in some conditions.^[11a,15]

The relaxation times of magnetization in DyLu₂N@C₈₀ and Dy₂LuN@C₈₀ in this work were determined at different temperatures by magnetizing the sample to saturation, quickly sweeping the magnetic field to zero or any other required field value, and then following the decay of magnetization with subsequent fitting of the measured decay curves with a stretched exponential (see the Supporting Information for the decay curves and Tables containing all the fitted parameters). Below, the values obtained here are compared with those of DySc₂N@C₈₀ from ref. [6b], whereas the relaxation times in Dy₂ScN@C₈₀ were re-measured in this work for better consistency.

The zero-field measurements for DyLu₂N@C₈₀ are complicated by the relatively long stabilization of the field and fast zero-field QTM. In addition, the decay curves showed two types of behavior: A fast drop of magnetization for around 90% of the sample, followed by a much slower relaxation of the remaining magnetization. The fit of the decay curves with two stretched exponents gave values ranging from 54 ± 1 s at 1.8 K to 21 ± 6 s at 5 K for the fast process (Figure 4a), which we assigned to QTM. The abrupt change in the relaxation rate may be caused by the redistribution of dipolar fields in the sample when a significant number of spins flip, the dilution effect of Lu₃N@C₈₀, and may also reflect different relaxation of the molecules with different dysprosium isotopes. In addition, the slow process may also be caused by slow relaxation of the remnant magnetization in the magnet, or the deviation of the real magnetic field from zero. For comparison, τ_{QTM} in nondiluted DySc₂N@C₈₀ determined by AC magnetometry in the same temperature range is 1–3 s.^[6b] Overall, we can conclude that the rate of relaxation by the QTM mechanism in DyLu₂N@C₈₀ is slower than in DySc₂N@C₈₀. Note that both compounds show a temperature dependence of the relaxation rate, even in the QTM regime, which may reflect the temperature dependence of the phonon collision rate, as suggested by Chilton and co-workers,^[16] or result from dipolar intermolecular interactions.

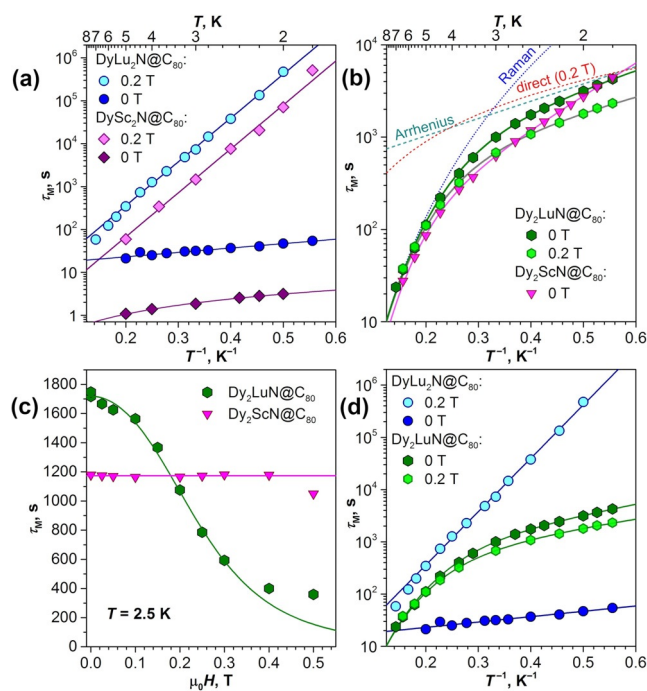


Figure 4. (a) Magnetization relaxation times of DyLu₂N@C₈₀ measured in zero field and in a field of 0.2 T and compared with those of DySc₂N@C₈₀ from ref. [6b] (the zero-field values for DySc₂N@C₈₀ were measured by AC magnetometry). The lines are fits of the Arrhenius behavior. (b) Magnetization relaxation times of DyLu₂N@C₈₀ measured in zero field and in a field of 0.2 T and compared with the relaxation times of Dy₂ScN@C₈₀ in zero field. The solid lines are total fits with Equations (4) and (5) (0 and 0.2 T, respectively). The contributions of the Arrhenius, Raman, and direct (for 0.2 T) processes are also shown. (c) Field dependence of magnetization relaxation times of Dy₂LuN@C₈₀ and Dy₂ScN@C₈₀ measured at 2.5 K. The green line is the fit of Dy₂LuN@C₈₀ data with Equation (1). (d) Comparison of the magnetization relaxation times of DyLu₂N@C₈₀ and Dy₂LuN@C₈₀.

Short relaxation times cannot be measured very reliably by DC magnetometry, and further relaxation measurements were performed for DyLu₂N@C₈₀ in a field of 0.2 T, applied to quench the QTM. Over a range of only 5 K, the in-field relaxation times in DyLu₂N@C₈₀ vary by almost four orders of magnitude, from 4.7×10^5 s at 2 K to 58 s at 7 K (Figure 4a). When plotted in Arrhenius coordinates, the temperature dependence of the relaxation times has a linear form below 5 K. For com-

parison, the τ_M values of DySc₂N@C₈₀ are systematically shorter than those of DyLu₂N@C₈₀ by a factor of six, but they also show a linear temperature dependence with a very similar inclination (Figure 4a). Fitting the relaxation times of DyLu₂N@C₈₀ with Equation (3) gave a U^{eff} value of 24.2 ± 0.7 K and τ_0 of 2.8 ± 0.5 s. The analogous fit for DySc₂N@C₈₀ gave $U^{\text{eff}} = 23.6 \pm 1$ K and $\tau_0 = 0.6 \pm 0.2$ s.^[6b] Thus, both NCFs have essentially identical U^{eff} values and differ only in their attempt times. The reason for the low-temperature U^{eff} barriers of 24 K in both DyM₂N@C₈₀ molecules is not clear. Due to the very strong LF splitting of dysprosium in the NCFs, the energies of the lowest-energy excited states exceed hundreds of K (see the discussion of the ab initio calculations below).^[2a-d,f,g] In addition, the τ_0 values are many orders of magnitude longer than are usually found for the Orbach mechanism. We tentatively propose that the relaxation of magnetization in SMM EMFs in this temperature range may follow the Raman mechanism with involvement of local vibrations that would also follow Equation (3), but with U^{eff} corresponding to the vibrational frequency.^[14a,17] The vibrational density of states in dysprosium NCFs is discussed further below.

The temperature dependence of the relaxation times of Dy₂LuN@C₈₀ measured in zero magnetic field has a curved shape in the log(τ_M) versus T^{-1} plot (Figure 4b) and can be described well by using a combination of Raman and Arrhenius processes, expressed by Equation (4).

$$\tau_M^{-1}(T) = CT^{n_1} + \tau_0^{-1} \exp(-U^{\text{eff}}/T) \quad (4)$$

The fit of the experimental zero-field relaxation times of Dy₂LuN@C₈₀ with Equation (4) gives $C = (1.14 \pm 0.28) \times 10^{-6} \text{ s}^{-1} \text{ K}^{-5.45}$, $n_1 = 5.45 \pm 0.15$, $\tau_0 = 435 \pm 50$ s, and $U^{\text{eff}} = 4.3 \pm 0.2$ K (Table 1). The Raman mechanism dominates above 4 K, whereas Arrhenius behavior is predominant below 2.5 K, and both mechanisms make comparable contributions in between. As for DyLu₂N@C₈₀, neither τ_0 nor U^{eff} of the Arrhenius part is typical for the standard Orbach relaxation process via ligand-field excited states. Spin relaxation in Dy₂ScN@C₈₀ below 8 K can be also described by Equation (4) with $C = (0.51 \pm 0.26) \times 10^{-6} \text{ s}^{-1} \text{ K}^{-5.99}$, $n_1 = 5.99 \pm 0.33$, $\tau_0 = 56 \pm 4$ s, and $U^{\text{eff}} = 8.0 \pm 0.1$ K (somewhat different values, $\tau_0 = 11.9 \pm 1.5$ s and $U^{\text{eff}} = 10.7 \pm 0.3$ K, reported by us in ref. [2d], were obtained with a smaller

	QTM τ_{QTM}^{-1}	Raman CT^{n_1}	Arrhenius $\tau_0^{-1} \exp(-U^{\text{eff}}/T)$	Direct $A(H)T^{n_2}$			
M ₃ N@C ₈₀ , field	τ_{QTM} [s]	C [$10^{-6} \text{ s}^{-1} \text{ K}^{-n_1}$]	n_1	τ_0 [s]	U^{eff} [K]	$A(H)$ [$10^{-5} \text{ s}^{-1} \text{ K}^{-n_2}$]	n_2
DyLu ₂ N, 0 T	20–50	–	–	–	–	–	–
DyLu ₂ N, 0.2 T	–	–	–	2.8 ± 0.5	24.2 ± 0.7	–	–
DySc ₂ N, 0 T	1–3	–	–	–	–	–	–
DySc ₂ N, 0.2 T	–	–	–	0.6 ± 0.2	23.6 ± 1.0	–	–
Dy ₂ LuN, 0 T	–	1.14 ± 0.28	5.45 ± 0.15	435 ± 50	4.3 ± 0.2	–	–
Dy ₂ LuN, 0.2 T	–	1.14 ± 0.28	5.45 ± 0.15	435 ± 50	4.3 ± 0.2	7.59 ± 0.57	1.67 ± 0.09
Dy ₂ ScN, 0 T	–	0.51 ± 0.26	5.99 ± 0.33	56 ± 4	8.0 ± 0.1	–	–

[a] Below T_B .

data set). Thus, Dy₂LuN@C₈₀ and Dy₂ScN@C₈₀ have similar parameters in the Raman process, but are significantly different in their Arrhenius behavior, as Dy₂ScN@C₈₀ has a two-fold higher U^{eff} and an eight-fold shorter τ_0 . As a result, although the zero-field relaxation times of Dy₂LuN@C₈₀ and Dy₂ScN@C₈₀ are very similar at 1.8 K and virtually identical by 7 K, between 2 and 6 K the relaxation of magnetization in Dy₂LuN@C₈₀ is considerably slower.

Measurements of magnetization relaxation times in Dy₂LuN@C₈₀ at 2.5 K in different magnetic fields (Figure 4c) revealed considerable acceleration of the relaxation with increasing field. The temperature dependence of the relaxation times measured in a field of 0.2 T also showed noticeable deviations from zero-field values below 5 K (Figure 4b). Such a dependence of τ_M on the magnetic field is a characteristic of the direct relaxation mechanism [Eq. (1)]. To describe the temperature dependence of the relaxation times measured in a field of 0.2 T, we used Equation (4) with the addition of a term describing the direct process, given by Equation (5)

$$\tau_M^{-1}(T) = CT^{n_1} + \tau_0^{-1} \exp(-U^{\text{eff}}/T) + A(H)T^{n_2} \quad (5)$$

in which C , n_1 , τ_0 , and U^{eff} were fixed to the values determined for zero-field relaxation.

The fit of the experimental data measured in a field of 0.2 T with Equation (5) gives $A(H) = (7.59 \pm 0.57) \times 10^{-5} \text{ s}^{-1} \text{ K}^{-1.67}$ and $n_2 = 1.67 \pm 0.09$ (Table 1). The exponent of approximately 1.7 lies between the values expected for normal ($n=1$) and bottleneck ($n=2$) direct processes, and indicates that both are likely to take place. If instead of using the fitting procedure, the n_2 value is fixed to 1 and $A(H)$ is determined from the field dependence at 2.5 K by using Equation (1) (Figure 4c), then Equation (5) describes well the temperature dependence above 2.5 K, but shows increasing deviations at lower temperature. This indicates that the bottleneck process has higher impact at low temperatures, when the number of excited phonons is not sufficient for efficient energy transfer. Note that the direct and Arrhenius processes in Dy₂LuN@C₈₀ have similar rates at 0.2 T, and hence in-field relaxation rates are around twice as fast up to 3 K, when the Raman process starts to dominate, and the field dependence eventually vanishes by 5 K.

In striking contrast to Dy₂LuN@C₈₀, the relaxation times of Dy₂ScN@C₈₀ at 2.5 K do not depend on the external magnetic field until it exceeds 0.4 T (Figure 4c). The relaxation times of Dy₂ScN@C₈₀ measured at different temperatures in a field of 0.2 T almost coincide with the zero-field values and start to show small deviations only below 2 K. This shows that the direct mechanism contributes to the spin relaxation in Dy₂ScN@C₈₀ at considerably higher fields and lower temperatures than in Dy₂LuN@C₈₀, which explains why the coercive field in the magnetic hysteresis of Dy₂ScN@C₈₀ is larger than in Dy₂LuN@C₈₀ (Figure 3b).

The temperature dependencies of the relaxation times of DyLu₂N@C₈₀ and Dy₂LuN@C₈₀ measured in zero field and in a field of 0.2 T are compared in Figure 4d. Once the QTM in DyLu₂N@C₈₀ is quenched by the application of a finite field, its relaxation rate is much slower than in Dy₂LuN@C₈₀, and at 2 K

the difference between mono- and di-dysprosium NCFs exceeds two orders of magnitude. Intramolecular interactions between dysprosium spins in Dy₂MN@C₈₀ block zero-field QTM and create a manifold of new low-energy coupled spin states. Apparently, spin relaxation in Dy₂LuN@C₈₀ at low temperature proceeds via such coupled states and is therefore much faster than in DyLu₂N@C₈₀, which has only single-ion excited spin states. A similar difference in the low-temperature relaxation mechanisms was also observed for DySc₂N@C₈₀ and Dy₂ScN@C₈₀.^[3a,6b] If indeed this is the case, the U^{eff} of the Arrhenius process in Dy₂MN@C₈₀ may be related to the energy difference between the ground and the first excited state of the coupled spin system. At higher temperature, the relaxation rates of DyM₂N@C₈₀ and Dy₂MN@C₈₀ tend to be more similar, which indicates that relaxation via single-ion states becomes equally efficient for both types of NCFs.

Single-ion anisotropy of dysprosium ions in DyM₂N@C₈₀ and Dy₂MN@C₈₀ (M = Sc, Lu)

The central nitride ion is the main source of the magnetic anisotropy in lanthanide NCFs, and the LF is expected to become stronger with decreasing distance between N³⁻ and Dy³⁺. DFT calculations at the PBE level with the 4f-in-core effective potential showed that the increase in the ionic radius from Sc³⁺ to Lu³⁺ shortens the Dy–N bond from 2.156 Å in DySc₂N@C₈₀ to 2.090 Å in DyLu₂N@C₈₀.^[8c] Likewise, the DFT-optimized Dy–N bonds in Dy₂LuN@C₈₀ (2.073 and 2.074 Å) are shorter than those in Dy₂ScN@C₈₀ (2.105 and 2.108 Å). These geometrical changes may substantially affect the LF acting on the dysprosium ions.

To explore the influence of this effect, we performed ab initio CASSCF/RASSI calculations on the LF splitting in DyLu₂N@C₈₀ and Dy₂LuN@C₈₀ molecules and compared the results with those for the dysprosium-scandium analogues. For Dy₂MN@C₈₀ molecules, only one dysprosium ion was treated ab initio at a time, and the other dysprosium was replaced by yttrium. The energies of the Kramers doublets (KDs) in DyM₂N@C₈₀ molecules, the pseudo-spin g -tensor of the ground state KD, and the transition probability in the first KD are presented in Figure 5, Table 2, and Table S7 in the Supporting Information. The calculations show that the Dy³⁺ ions in DyLu₂N@C₈₀ and Dy₂LuN@C₈₀ exhibit high magnetic anisotropy with overall LF splitting of 1340–1360 cm⁻¹. The quantization axis is aligned along the Dy–N bond, and the ground Kramers doublet is described as an essentially pure state with $|m_j| = 15/2$. The energy of the second Kramers doublet is predicted to be close to 400 cm⁻¹, which ensures that the low-temperature magnetic properties of both DyLu₂N@C₈₀ and Dy₂LuN@C₈₀ are determined solely by the ground state of Dy³⁺, as in the previously studied dysprosium-scandium NCFs.^[2d,3a,6b,d] A comparison of DySc₂N@C₈₀ and DyLu₂N@C₈₀ shows that the increase in metal size from scandium to lutetium leads to an increase in LF splitting from 1284 cm⁻¹ (DySc₂N) to 1348 cm⁻¹ (DyLu₂N). The energy of the second KD (relative to the first KD) also shows an increase from 356 cm⁻¹ in DySc₂N@C₈₀ to 391 cm⁻¹ in DyLu₂N@C₈₀. As the Dy–N bonds in Dy₂LuN@C₈₀

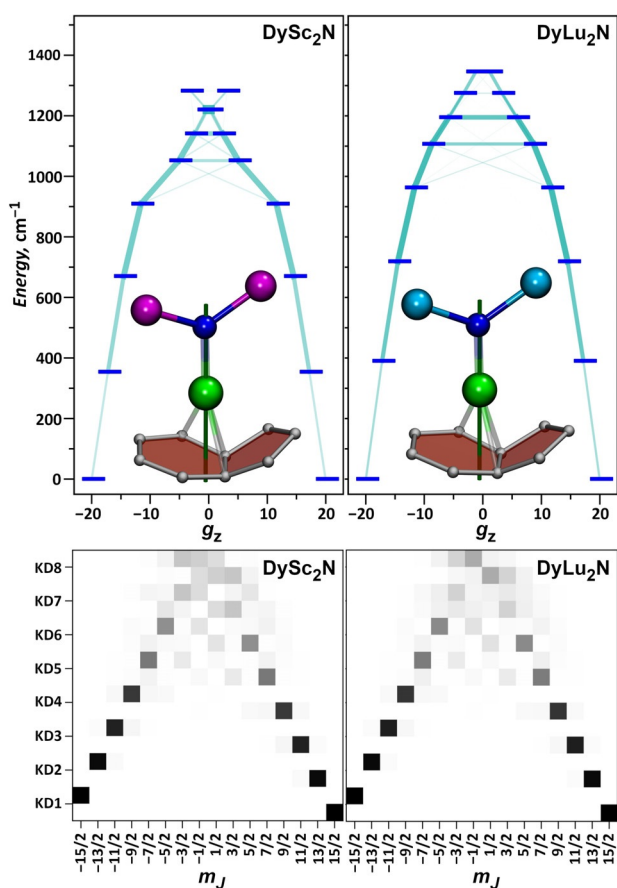


Figure 5. Top: Ab initio computed LF splitting for Dy³⁺ in DySc₂N@C₈₀ and DyLu₂N@C₈₀ molecules. The light-blue lines visualize the transition probabilities between the KD states. Also shown are DyM₂N clusters (Dy, green; Sc, magenta; N, blue; Lu, cyan) with the Dy-coordinated fragment of the fullerene cage (Dy–C distances shorter than 2.4 Å are visualized as bonds). The quantization axis determined by ab initio calculations is shown as a dark-green line. Bottom: Visualization of the KD wave-function composition in the $|15/2, m_j\rangle$ basis (see Table S7 in the Supporting Information for numerical data).

are somewhat shorter than that in DyLu₂N@C₈₀, the LF splitting for the dysprosium ion in the former is also slightly higher. Likewise, the LF splitting in Dy₂LuN@C₈₀ is somewhat higher than in Dy₂ScN@C₈₀, which also correlates with the shorter Dy–N bond lengths (see Tables S8 and S9).

For the relaxation of magnetization, not only the energies of the KD states, but also the transition probabilities between them as well as the composition of the wave functions in the $|J, m_j\rangle$ basis are very important (Figure 5, see also Table S7 in the Supporting Information). The first KD with g_z close to 19.8 and infinitesimally small g_x and g_y values has more than 99% contribution from the $|m_j| = 15/2$ function for all the discussed NCFs. The probability of a QTM transition within the first KD is only $1.1 \times 10^{-9} \mu_B^2$ in DySc₂N@C₈₀ and $1.7 \times 10^{-9} \mu_B^2$ in DyLu₂N@C₈₀. The QTM transition probabilities within one KD remain low up to the fourth KD (Figure 5), and similar values are also found for Dy₂MN@C₈₀ molecules. Likewise, transitions between the states of different m_j and opposite spin are also not efficient until KD4. The reasons for this situation are rooted in the composition of the KD wave functions, which can be de-

scribed as essentially pure m_j states up to KD4–KD5 (Figure 5). Thus, ab initio calculations predict that the relaxation of magnetization in all dysprosium NCFs should proceed via the KD5, as indeed was observed experimentally in Dy₂ScN@C₈₀.^[2d] There is no considerable difference between dysprosium-scandium and dysprosium-lutetium nitride clusterfullerenes in this regard.

To summarize, the replacement of scandium by lutetium in mixed-metal nitride clusterfullerenes shortens the Dy–N bonds and increases the LF splitting by 5–10%. Otherwise, there is no significant difference in terms of KD composition and the expected relaxation pathways via excited KDs.

Intramolecular interactions of dysprosium magnetic moments in Dy₂LuN@C₈₀

The system of two weakly interacting dysprosium centers with magnetic moments $\hat{J}_{1,2}$ can be described by the effective spin Hamiltonian given by Equation (6)

$$\hat{H}_{\text{spin}} = \hat{H}_{\text{LF}_1} + \hat{H}_{\text{LF}_2} - 2j_{1,2}\hat{J}_1\hat{J}_2 \quad (6)$$

in which \hat{H}_{LF_i} is the single-ion LF Hamiltonian for the i th dysprosium site, dysprosium moments \hat{J}_i are treated in the $|J, m_j\rangle$ basis, and $j_{1,2}$ is the coupling constant between the localized dysprosium moments. Here, $j_{1,2}$ is treated isotropically in the spirit of the Lines model^[18] and includes both exchange and dipolar interactions.

To determine the $j_{1,2}$ constant for Dy₂LuN@C₈₀, we simulated magnetization curves with different values of $j_{1,2}$ and compared them with the experimental data. In these simulations the angle, α , between the single-ion anisotropy axes of the dysprosium ions is set to 61.7°, as determined by ab initio calculations. The best agreement is achieved for $j_{1,2} = 0.02$ – 0.03 cm^{-1} (Figure 6). As follows from Equation (6), for the two dysprosium spins oriented at an angle of $\alpha = 61.7^\circ$, the energy difference between the states with ferromagnetic (FM) and antiferromagnetic (AF) coupling of the dysprosium ions ($J = 15/2$) can be calculated from Equation (7)

$$\Delta E_{\text{FM-AF}} = 4j_{1,2}J^2\cos(\alpha) = 225j_{1,2}\cos(\alpha) \quad (7)$$

which gives an estimation of 2.1–3.2 cm⁻¹ (3.1–4.6 K) for Dy₂LuN@C₈₀. This energy difference is close to the U^{eff} value of 4.3 K determined for the low-temperature relaxation process with Arrhenius behavior (see above). The assumption that the relaxation proceeds by excitation to the antiferromagnetically coupled state (i.e., $\Delta E_{\text{FM-AF}} = U^{\text{eff}}$)^[2e,3a] allows a more precise estimation of $j_{1,2} = 0.028 \pm 0.001 \text{ cm}^{-1}$. This value also gives a reasonable agreement between the experimental and simulated χT curves (see Figure S8 in the Supporting Information).

Magnetic Dy...Dy interactions have two components, dipolar and exchange. The energy difference between the dipolar interactions in the FM and AF states, $\Delta E_{\text{FM-AF}}^{\text{dip}}$, can be calculated by using the well-known formula for the energy of dipolar interactions between two magnetic moments [Eq. 8],

Table 2. Ligand-field splitting of the Dy³⁺ states and the ground-state *g*-tensor in DyM₂N@C₈₀ and Dy₂MN@C₈₀ (M = Sc, Lu) molecules as predicted by ab initio calculations.

	DySc ₂ N	DyLu ₂ N	Dy ₂ ScN		Dy ₂ LuN	
			Dy1	Dy2	Dy1	Dy2
KD1 [cm ⁻¹]	0	0	0	0	0	0
KD2 [cm ⁻¹]	356	391	399	378	408	403
KD3 [cm ⁻¹]	666	715	704	698	726	726
KD4 [cm ⁻¹]	906	960	938	945	967	971
KD5 [cm ⁻¹]	1050	1104	1081	1084	1109	1112
KD6 [cm ⁻¹]	1140	1194	1176	1174	1203	1202
KD7 [cm ⁻¹]	1222	1276	1253	1263	1283	1286
KD8 [cm ⁻¹]	1284	1348	1336	1333	1365	1366
<i>g_x</i>	0.00005	0.00006	0.00006	0.00004	0.00007	0.00007
<i>g_y</i>	0.00006	0.00007	0.00008	0.00006	0.00008	0.00008
<i>g_z</i>	19.83868	19.83507	19.87022	19.85862	19.82302	19.85935
β ^[a] [°]	1.6	1.8	2.2	2.0	2.2	2.1
KD1 ↔ KD1' [μ _B ²]	1.1 × 10 ⁻⁹	1.7 × 10 ⁻⁹	2.5 × 10 ⁻⁹	8.0 × 10 ⁻¹⁰	2.4 × 10 ⁻⁹	2.4 × 10 ⁻⁹
<i>d</i> (Dy–N) ^[c] [Å]	2.156	2.090	2.105	2.108	2.074	2.073

[a] β is the angle between the Dy–N bonds and the quantization axis of the Dy ions. [b] KD1 ↔ KD1' denotes the transition probability between the two degenerate states in the first KD, that is, the probability of QTM. [c] The Dy–N bond lengths correspond to the DFT-optimized structures, see ref. [8c] for a comparison of the experimental and computed Dy–N distances.

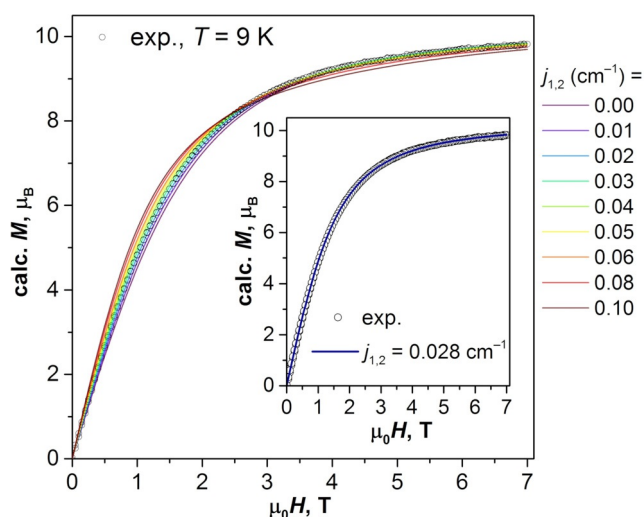


Figure 6. Experimental magnetization curve of Dy₂LuN@C₈₀ measured at 9 K (dotted line) compared with the curves simulated using Equation (5) with different values of *j*_{1,2} from 0 to 0.1 cm⁻¹. The inset compares the experimental curve with the simulated one for *j*_{1,2} = 0.028 cm⁻¹.

$$E_{1,2}^{\text{dip}} = -\frac{\mu_0}{4\pi R_{1,2}^3} [3(\vec{n}_r, \vec{\mu}_1)(\vec{n}_r, \vec{\mu}_2) - (\vec{\mu}_1, \vec{\mu}_2)] \quad (8)$$

in which \vec{n}_r is the normal of the radius vector connecting the two magnetic moments $\vec{\mu}_1$ and $\vec{\mu}_2$, $R_{1,2}$ is the distance between them, and μ_0 is the vacuum permeability. For Dy₂LuN@C₈₀ with DFT-optimized coordinates and $|\vec{\mu}_{1,2}| = 10 \mu_B$, Equation (8) gives $\Delta E_{\text{FM-AF}}^{\text{dip}} = 4.8$ K. Surprisingly, it appears that the Dy...Dy interactions in Dy₂LuN@C₈₀ are solely of dipolar nature, with the exchange term vanishing almost completely. For Dy₂ScN@C₈₀, Equation (8) gives a very similar value of

$\Delta E_{\text{FM-AF}}^{\text{dip}} = 4.7$ K, but as the $\Delta E_{\text{FM-AF}}$ energy in Dy₂ScN@C₈₀ is twice as large as in Dy₂LuN@C₈₀, one can conclude that the exchange term for Dy₂ScN@C₈₀ is of a similar size to the dipolar term (Table 3). Thus, substitution of scandium by lutetium in the Dy₂MN cluster results in considerable variation of the coupling constant, mainly because of the negligible exchange interactions in Dy₂LuN@C₈₀, which also leads to a smaller energy difference between the ferromagnetically and antiferromagnetically coupled states, and through this difference has a strong influence on the relaxation of magnetization at low temperature.

Table 3. Exchange and dipolar coupling parameters for di-Dy EMFs.

	$\Delta E_{\text{FM-AF}}^{\text{[a]}}$ [K]	$\Delta E_{\text{FM-AF}}^{\text{dip}}$ [K]	<i>j</i> _{1,2} [cm ⁻¹]	α ^[b] [°]	<i>R</i> ₁₂ ^[c] [Å]
Dy ₂ LuN@C ₈₀	4.3 ± 0.2	4.8	0.028	61.7	3.559
Dy ₂ ScN@C ₈₀	8.0 ± 0.1 ^[d]	4.7	0.055	63.4	3.576

[a] $\Delta E_{\text{FM-AF}}$ is considered to be equal to U^{eff} of the low-temperature Arrhenius process. [b] α is the angle between the quantization axes of two Dy ions, determined from ab initio calculations. [c] *R*₁₂ is the distance between two Dy ions in DFT-optimized molecules. [d] The more precise measurements in this work give a somewhat different value from our previous report in ref. [2d] and are closer to the data reported earlier in ref. [3a].

Low-frequency molecular and lattice vibrations in dysprosium-metal NCFs

As follows from the ab initio calculations discussed above, dysprosium-scandium and dysprosium-lutetium NCFs have very similar single-ion magnetic anisotropy and ground-state properties. In addition, the LF splitting in these NCFs is very large and is not relevant for the low-temperature relaxation of magnetization. Therefore, the difference in their relaxation behavior

cannot be explained by the LF splitting and it is necessary to take into account other factors. In addition, the observation of Arrhenius behavior in $\text{DySc}_2\text{N@C}_{80}$ and $\text{DyLu}_2\text{N@C}_{80}$ with a U^{eff} of 24 K and unconventional parameters also cannot be explained by LF splitting. A deeper insight into the spin–phonon interactions may be needed to explain these phenomena.

The drawbacks of the commonly applied phenomenological approaches to spin–phonon interactions developed in the 1960s are that they are based on the Debye model for vibrations in the crystal and do not provide a clear connection with the microscopic parameters of the molecules (except for the LF splitting, when the Orbach process is involved). For instance, although the relaxation times measured in this work can be well fitted by Equations (1)–(3) and their combinations, the fitted parameters do not provide sufficient insight into the relation between molecular structure and the relaxation of magnetization.

Recently, Lunghi et al.^[17] analyzed spin–lattice relaxation in molecular magnets by using quantum spin dynamics, considering explicit vibrations of the molecule and deriving the spin–phonon coupling parameters from ab initio calculations. They found that spin–phonon relaxation via anharmonic phonons may also result in Arrhenius behavior, but with the U^{eff} corresponding to half of the vibrational frequency. Furthermore, other research teams analyzed the locality of the spin–phonon interaction and concluded that molecular vibrations spatially localized close to the metal center usually have the strongest contribution to the spin relaxation.^[17,19] These findings show that the Debye model is oversimplified for the analysis of spin–phonon relaxation in molecular magnets^[20] and an analysis of the real vibrational spectra may give better insight into the relaxation mechanism.^[21] With this in mind, we decided to analyze the low-frequency part of the vibrational spectra of the NCFs. The experimental Raman spectra of $\text{DyM}_2\text{N@C}_{80}$ and $\text{Dy}_2\text{MN@C}_{80}$ ($M = \text{Sc}, \text{Lu}$; limited to frequencies above 50 cm^{-1} due to instrument limitations) are compared in Figure 7 with the vibrational density of states (VDOS), computed by DFT for isolated molecules. In addition to the total VDOS, Figure 7 also shows contributions to the VDOS of the whole metal nitride cluster and of only the dysprosium atoms. The computed and

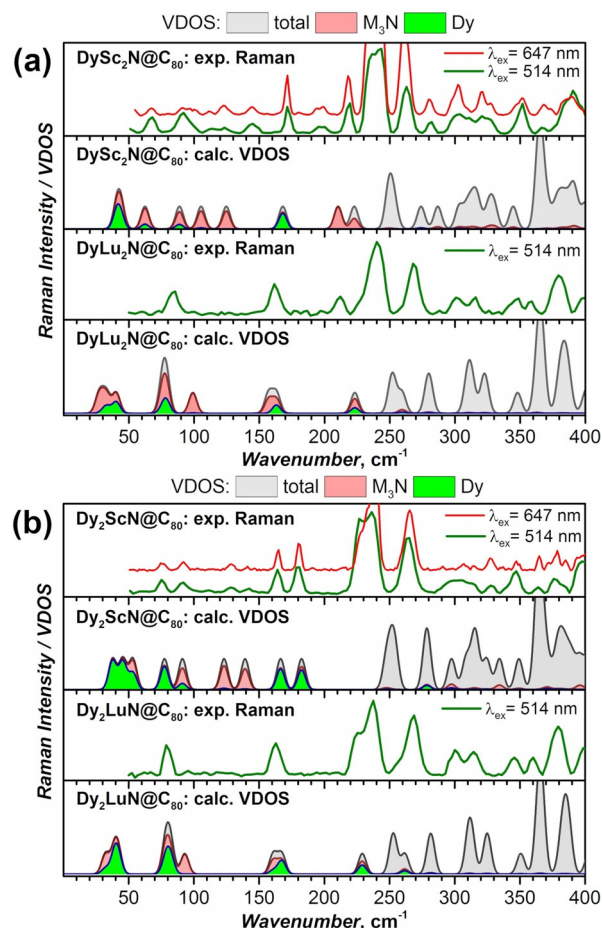


Figure 7. Raman spectra ($T = 77 \text{ K}$, $\lambda_{\text{ex}} = 514$ or 647 nm) and DFT-calculated VDOS for (a) $\text{DyM}_2\text{N@C}_{80}$ and (b) $\text{Dy}_2\text{MN@C}_{80}$ ($M = \text{Sc}, \text{Lu}$). The total VDOS is shown in gray, and the contributions to the VDOS of the whole M_3N cluster and of the Dy atoms are shown in pink and green, respectively.

experimental frequencies of the cluster-based modes are presented in Table 4.

EMFs have rather peculiar vibrational spectra as their molecules consist of two semi-independent units, the vibrations of which show almost no overlap in the energy scale, as can be

Table 4. Experimental and DFT-computed frequencies of cluster-based vibrations in $\text{DyM}_2\text{N@C}_{80}$ and $\text{Dy}_2\text{MN@C}_{80}$ ($M = \text{Sc}, \text{Lu}$). ^[a]											
		Vibrational frequency [cm^{-1}]									
Calcd	$\text{DySc}_2\text{N}^{[b]}$			Dy_2ScN			DyLu_2N			Dy_2LuN	
	Exp		Calcd	Exp	Calcd	Exp	Calcd	Exp	Calcd	Exp	
41		R	38		$\text{R}_{\text{Sc-N}}$	27		$\text{R}_{\text{Dy-N}}$	32		R
44		R	45		R	33		R	39		R
62	67	$\text{R}_{\text{Dy-N}}$	53		R	40		R	42		R
89	91	$\text{T} + \delta_{\text{DyNSc}}$	77	75	δ_{DyNDy}	75	84	$\text{T} + \delta_{\text{LuNLu}}$	78	79	δ_{DyNLu}
105	111	$\text{T} + \delta_{\text{DyNSc}}$	91	91	T	78	84	$\text{T} + \delta_{\text{LuNLu}}$	80	79	$\text{T} + \delta_{\text{DyNDy}}$
125	122	δ_{ScNSc}	123	129	δ_{DyNSc}	79	84	δ_{DyNLu}	82	79	$\text{T} + \delta_{\text{DyNDy}}$
168	172	$\text{T} + \nu_{\text{Dy-N}}$	139	142	γ_{N}	99		γ_{N}	93		γ_{N}
210	198	γ_{N}	167	164	$\text{T} + \delta_{\text{DyNDy}}$	157	162	$\text{T} + \nu_{\text{Lu-N}}$	161	163	$\text{T} + \nu_{\text{Lu-N}}$
223	218	$\text{T} + \delta_{\text{DyNSc}}$	183	180	$\text{T} + \nu_{\text{Dy-N}}$	163	162	$\text{T} + \nu_{\text{Dy-N}}$	167	163	$\text{T} + \nu_{\text{Dy-N}}$
						223	212	$\nu_{\text{M-N}}$	229		$\nu_{\text{M-N}}$

[a] Designation of cluster modes: R, rotation (libration); T, translation; $\delta_{\text{MNM}'}$, M–N–M' bending; γ_{N} , nitrogen out-of-plane displacement; $\nu_{\text{M-N}}$, M–N stretching vibration. [b] Experimental Raman spectrum of $\text{DySc}_2\text{N@C}_{80}$ has a peak at 145 cm^{-1} that cannot be assigned on the basis of calculation results.

well seen in Figure 7. Thus, the vibrations of the relatively rigid carbon cage occur at frequencies exceeding 240 cm^{-1} , whereas the frequencies of metal-involving modes rarely exceed 230 cm^{-1} , because the metal atoms are much heavier than carbon atoms. Only in the border range of $220\text{--}260\text{ cm}^{-1}$ do the squashing cage modes partially mix with the “breathing” mode of the nitride cluster, in which all three metal atoms move radially in one phase along the M–N bonds. Other metal-based vibrations occur at frequencies below 200 cm^{-1} . When the nitride cluster is encapsulated inside the fullerene, its external degrees of freedom (i.e., translations and rotations) are transformed into internal ones (i.e., molecular vibrations). The frustrated rotations (i.e., librations) are the lowest-frequency intramolecular modes predicted to be close to $30\text{--}40\text{ cm}^{-1}$ in dysprosium-lutetium NCFs and at $40\text{--}60\text{ cm}^{-1}$ in dysprosium-scandium NCFs. The frustrated translations are mixed with deformations of the cluster (such as in-plane oscillations of the M–N–M angles). In $\text{DyLu}_2\text{N@C}_{80}$ and $\text{Dy}_2\text{LuN@C}_{80}$, these modes are clustered into two groups close to 80 and 160 cm^{-1} (because dysprosium and lutetium have similar atomic masses, both dysprosium-lutetium NCFs have very similar VDOS). In dysprosium-scandium NCFs, such modes are more uniformly spread in the $80\text{--}200\text{ cm}^{-1}$ range. Finally, the nitrogen out-of-plane mode also falls in the range of $90\text{--}210\text{ cm}^{-1}$.

The results of the computations agree reasonably well with the experimental Raman spectra. Above 220 cm^{-1} , the spectra of all the NCFs are quasi-continuous because of densely spaced cage vibrations. The calculations seem to overestimate the cage frequencies by around 10%. In the cluster frequency range, $\text{DyLu}_2\text{N@C}_{80}$ and $\text{Dy}_2\text{LuN@C}_{80}$ exhibit only two Raman peaks, at around 80 and 162 cm^{-1} , close to the predicted frequencies of the mixed translation/deformation modes. The dysprosium-scandium NCFs exhibit richer spectral patterns, and most of the observed peaks can be reliably assigned to the computed modes, as listed in Table 4 (see refs. [22] for a more detailed discussion of the vibrational spectra of $\text{MSc}_2\text{N@C}_{80}$ NCFs). Due to technical limitations, we cannot record the spectra below 50 cm^{-1} , which precludes experimental observation of the cluster librations in dysprosium-lutetium NCFs. However, good agreement between experiment and theory for the cluster modes above 50 cm^{-1} ensures that the calculated frequencies are not far from reality. In addition, in some of the earlier Raman studies of the NCFs, peaks at around $30\text{--}40\text{ cm}^{-1}$ were reported for $\text{Dy}_3\text{N@C}_{80}$, $\text{Lu}_3\text{N@C}_{80}$, and some other $\text{M}_3\text{N@C}_{80}$ molecules.^[8a, 23]

Librations of the cluster and lattice phonons in spin relaxation

The low-frequency vibrations localized on the metal nitride cluster of the $\text{M}_3\text{N@C}_{80}$ molecules are expected to mediate energy transfer between the spin and a thermal bath. The rotational motions of the cluster are especially of interest from the point of view of low-temperature spin relaxation because they not only happen at low frequencies (i.e., in the relevant energy range), but also because they may help to conserve the total angular momentum when the spin flips. The relevance of the

Einstein–de Haas effect on the single-molecule level was demonstrated by Wernsdorfer and co-workers for TbPc_2 (Pc = phthalocyanine) grafted on a carbon nanotube (CNT).^[24] To conserve the total momentum, the spin reversal of terbium had to result in rotation of the TbPc_2 molecule around the terbium quantization axis. However, because the molecule was rigidly bonded to the CNT, to fulfill the rotational invariance, the rotational momentum had to be transferred to the momentum of the phonon propagating along the nanotube. As a result, the efficient spin reversal proceeded by the direct mechanism when the external magnetic field created a Zeeman splitting matching the frequency of the longitudinal nanotube phonon. In a dysprosium nitride cluster, the reversal of the spin aligned along the Dy–N bond should induce rotation of the cluster around this bond. But as discussed above, interaction with the fullerene cage restricts the rotational motion of the cluster and turns it into a vibration, albeit retaining its rotational character. In $\text{DyLu}_2\text{N@C}_{80}$ and $\text{DySc}_2\text{N@C}_{80}$, the frequencies of the corresponding cluster librations are predicted at 27 and 62 cm^{-1} , respectively (Table 4). However, localized molecule vibrations at the Γ point do not transfer moment either, and hence their dispersions and interactions with lattice phonons should be studied further.

Consideration of the lattice phonons in EMF solids is also necessary because their frequency range is likely to overlap with low-frequency intramolecular vibrations. Unfortunately, experimental information on lattice phonons in EMFs is very limited. To the best of our knowledge, there has been only one study of monometallofullerenes by inelastic neutron scattering, which showed almost featureless VDOS in the low-frequency range.^[25] Far-IR^[25, 26] as well as the aforementioned Raman studies proved the presence of some low-frequency modes in EMFs, but metal-based intramolecular vibrations could not be distinguished from the lattice modes, and, in addition, the selection rules limit the optical activity only to the Γ point. Lattice vibrations of empty fullerenes, and especially C_{60} , are much better studied. According to inelastic neutron scattering and ab initio computations, the lattice phonons of C_{60} exhibit rather strong dispersion and cover the range up to $60\text{--}70\text{ cm}^{-1}$,^[27] whereas optical spectroscopic studies revealed the bands of librational modes at 7 and 18 cm^{-1} , and those of translational modes at 28 , 41 , and 59 cm^{-1} .^[28] Thus, we can tentatively suggest that the frequency ranges of lattice modes and the intramolecular cluster vibrations of EMFs do overlap, which may lead to significant mode mixing.

In the absence of experimental information, we performed computational modeling of the lattice phonons of $\text{M}_3\text{N@C}_{80}$ to analyze their possible interaction with intramolecular vibrations. Complete calculations of the phonons of fullerene crystals at the DFT level are hardly feasible at this moment, and therefore simulations were performed by using the less demanding density-functional based tight-binding (DFTB) approach.^[29] The pair-atomic interaction potentials available for $\text{Sc}_3\text{N@C}_{80}$ showed a reasonable prediction of the molecular geometry and vibrations.^[30] As potentials for other lanthanide atoms of interest are not known, we used the $\text{Sc}_3\text{N@C}_{80}$ model to determine the Hessian and then computed the dispersion

spectra and vibrational eigenvectors for different lanthanide-containing NCFs by using a proper mass correction in a dynamic matrix.

The model lattice of $M_3N@C_{80}$ molecules was simulated with face-centered cubic (FCC) packing with the optimized unit cell parameter a of 15.5 Å and the distance between the centers of fullerene molecules of 11 Å (see Figure S11 in the Supporting Information). The vibrational spectra computed for isolated $DySc_2N@C_{80}$ and $DyLu_2N@C_{80}$ molecules are compared in Figure 8 with those of the crystal phase, and dispersion of the phonons along the high-symmetry line Γ -X can be seen. In both cases, the DFTB-computed spectra of the isolated molecules start above 50 cm^{-1} , which is just on the borderline for the acoustic bands of the crystals. The molecular modes away from the frequency range of the acoustic modes show noticeable Davydov splitting but negligible k -dispersion. But the local modes close to the acoustic bands intertwine with the dispersed lattice bands giving rise to a dense phonon structure starting from zero frequency on. Three clear acoustic modes are perturbed by a set of what appear to be local modes with fluid character across k -space. To follow the possible mode mixing in k -space, we chose Γ -point vibrational eigenvectors as a basis space, in which eigenvectors computed at different k values were projected.

The results of this projection analysis for one pure acoustic mode and for one with cluster libration character are presented in Figure 8a,b using a color code (blue for the acoustic and

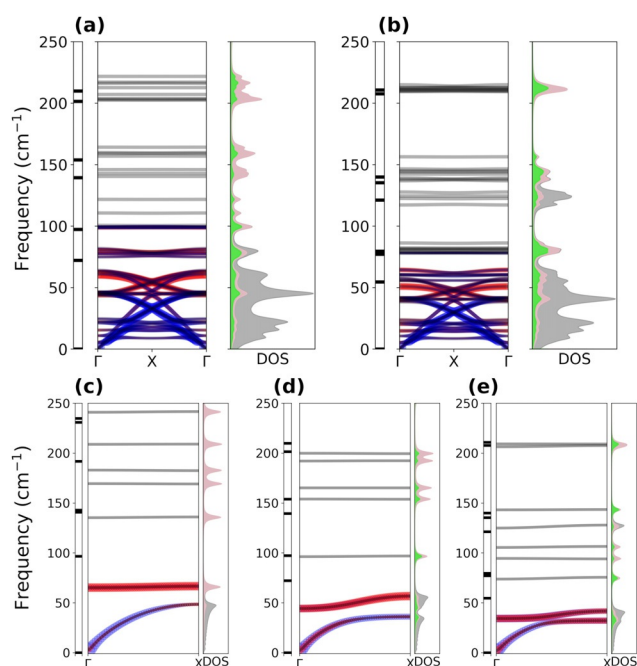


Figure 8. Phonon spectra for five model systems: 3D crystal with FCC packing of (a) $DySc_2N@C_{80}$ and (b) $DyLu_2N@C_{80}$; 1D chains of (c) $Sc_3N@C_{80}$, (d) $DySc_2N@C_{80}$, and (e) $DyLu_2N@C_{80}$. For each system, the right panel represents the frequencies computed for isolated molecules, the central panel shows phonon dispersions along the Γ -X high-symmetry path with information on band compositions (see text for details), and the left panel demonstrates the projected VDOS (total, gray; M_3N cluster, pink; Dy contribution, green).

red for the libration) and a scatter plot, for which the size of the dots is proportional to the magnitude of the projection (Figure 8). In this representation we can see and quantify how strongly the acoustic mode couples to more localized modes as a function of k . This redistribution is also reflected in the projected DOS in Figure 8, with the acoustic band showing a steady increase of cluster contributions as the energy increases. This model computation clearly shows that substantial mode mixing indeed takes place in k -space. However, the 3D model is challenging to grasp due to extensive mixing and a high density of states. For illustrative purposes, we simplified the model to one dimension and considered a linear chain of $M_3N@C_{80}$ molecules with $a=10.75$ Å (see Figure S11 in the Supporting Information).

Figure 8c–e shows dispersion relationships computed for 1D chains of three NCF molecules, namely $Sc_3N@C_{80}$, $DySc_2N@C_{80}$, and $DyLu_2N@C_{80}$. The spectra contain only one prominent acoustic band with a large dispersion of 50 cm^{-1} and two bands with a smaller dispersion of 10 cm^{-1} produced by on-site rotational degrees of freedom. In 1D $Sc_3N@C_{80}$, the lattice and cluster modes are high in frequency, the cluster libration band is flat, and a weak mixing with the acoustic mode can be detected only around the X symmetry point. With the increase in mass in $DySc_2N@C_{80}$, the cluster-based frequencies decrease faster than those of the lattice phonons, and the degree of mixing increases as manifested in the considerable dispersion of the intramolecular mode propelled by the acoustic band. Furthermore, the local and acoustic mode frequencies are even closer in 1D $DyLu_2N@C_{80}$, and therefore the mode mixing is much more pronounced.

The mixing of cluster libration modes with the lattice phonons outside of the Γ point has profound consequences for momentum transfer. These results show how in the first instance the librations, still being local modes, can assist the total conservation of momentum during spin flip and would be able to redistribute the excess angular momentum onto the lattice at some k values. Mixing of the cluster rotations with the lattice phonons thus facilitates spin reversal by interaction of the local and lattice modes in k -space. Based on this conclusion, we tentatively suggest that the Arrhenius behavior with a U^{eff} of 24 K (17 cm^{-1}) observed in the temperature dependence of magnetization relaxation times of $DySc_2N@C_{80}$ and $DyLu_2N@C_{80}$ (Figure 4a) may be caused by spin reversal assisted by the rotational modes of the M_3N cluster. U^{eff} in this case should correspond not to the frequency in the Γ point, but rather to the frequencies in the high density of states of the phonons with strong mixed character. In addition, the difference in the masses of the dysprosium-scandium and dysprosium-lutetium nitride clusters will result in a different degree of mixing between the cluster librations and lattice phonons, thus leading to a different efficiency of the spin–lattice relaxation.

Conclusions

In this work we have studied the magnetic properties of the nitride clusterfullerenes $DyLu_2N@C_{80}$ and $DyLuN@C_{80}$ and ana-

lyzed how substitution of scandium by lutetium in the mixed-metal clusterfullerenes $\text{DyM}_2\text{N@C}_{80}$ and $\text{Dy}_2\text{MN@C}_{80}$ affects the single-molecule magnetism thereof. $\text{DyLu}_2\text{N@C}_{80}$ and $\text{Dy}_2\text{LuN@C}_{80}$ have been found to be SMMs with a blocking temperature of 9.5 and 8 K, respectively. $\text{DyLu}_2\text{N@C}_{80}$ exhibits a higher blocking temperature, longer relaxation times, and broader hysteresis than the dysprosium-scandium analogue $\text{DySc}_2\text{N@C}_{80}$. Both $\text{DySc}_2\text{N@C}_{80}$ and $\text{DyLu}_2\text{N@C}_{80}$ feature zero-field QTM, and when the QTM is quenched in a finite field of 0.2 T, the magnetization relaxation times of both compounds show Arrhenius behavior with an effective barrier of 24 K.

$\text{Dy}_2\text{LuN@C}_{80}$ and $\text{Dy}_2\text{ScN@C}_{80}$ have identical blocking temperatures, but show different temperature and field dependence of the relaxation times. In particular, a direct relaxation mechanism with enhanced field dependence is observed for $\text{Dy}_2\text{LuN@C}_{80}$ below 5 K, whereas the relaxation times of $\text{Dy}_2\text{ScN@C}_{80}$ remain independent of field until the field exceeds 0.4 T. The magnetization relaxation times of $\text{Dy}_2\text{LuN@C}_{80}$ show Arrhenius behavior with an effective barrier of 4.3 K, which has been assigned to the energy of the excited state with antiferromagnetic coupling of the dysprosium moments, $\Delta E_{\text{FM-AF}}$. In $\text{Dy}_2\text{ScN@C}_{80}$, the energy of this state is around two-fold higher, at 8.0 K. Because $\text{Dy}_2\text{LuN@C}_{80}$ and $\text{Dy}_2\text{ScN@C}_{80}$ have almost identical energies of intramolecular dipolar interactions of 4.7 K, the considerable difference in their $\Delta E_{\text{FM-AF}}$ values is attributed to the strong variation in the exchange coupling when scandium is substituted by lutetium. Essentially, the magnetic moments in $\text{Dy}_2\text{LuN@C}_{80}$ show only dipolar interactions and their exchange coupling vanishes.

To aid the understanding of possible spin-phonon energy exchange, the low-frequency vibrational spectra of the dysprosium-lutetium and dysprosium-scandium NCFs were analyzed experimentally and with the help of DFT calculations. Enclosing the M_3N cluster inside the fullerene cage transforms its rotational degrees of freedom into molecular vibrations, which retain rotational character and are dubbed as librations of the cluster. The low frequencies of these modes lead to overlap with the frequency range of the lattice phonons. Furthermore, projection analysis also revealed the strong mixing of the local cluster librations with acoustic phonons of the fullerene lattice in the k -space away from the Γ point. As a result, these modes are predicted to facilitate the relaxation of magnetization by helping to conserve momentum during the spin reversal. Thus, the results of our study emphasize that the mixing of local and lattice modes in k -space may be an important mechanism of the spin-lattice relaxation and should be considered for other molecular magnets.

Experimental Section

Powder samples of fullerenes for magnetometry studies were prepared by drop-casting from toluene or CS_2 solutions. The magnetic properties were studied with a Quantum Design MPMS3 Vibrating Sample Magnetometer (VSM). Modeling of the magnetization curves and the spin Hamiltonian solution was accomplished with the PHI program.^[31]

Raman spectra were recorded at 77 K with a T 64000 triple spectrometer (Jobin Yvon) using an excitation wavelength of $\lambda_{\text{ex}} = 514$ nm (Ar^+ laser) or $\lambda_{\text{ex}} = 647$ nm (Kr^+ laser). The samples for Raman measurements were drop-cast onto single-crystal KBr disks. DFT calculations on isolated $\text{M}_3\text{N@C}_{80}$ molecules were performed at the PBE-D level with a plane-wave basis set and the corresponding projector augmented-wave potentials, treating 4f electrons as a part of the core as implemented in the VASP 5.0 package.^[32] These calculations employed a cubic unit cell with a lattice parameter of 25 Å and the atomic cut-off energy was set to 400 eV. The precision was set to be "accurate" with real-space projector operators optimized down to 10^{-4} eV per atom. The Γ -point Hessian matrix and then the vibration frequencies (or Γ -point phonons) were determined by using density functional perturbation theory as implemented in VASP.

The ab initio energies and wave functions of LF (ligand field) multiplets for the dysprosium-lutetium NCF molecules were calculated at the CASSCF/SO-RASSI level of theory with atomic natural orbital extended relativistic basis set (ANO-RCC)^[33] of the valence double-zeta (VDZ) quality using the quantum chemistry package MOLCAS 8.0.^[34] The active space of the CASSCF calculations included the 4f shell, that is, 11 active electrons and 7 active orbitals. All 21 sextet states and 108 quartets and only 100 doublets were included in the state-averaged CASSCF procedure and further used in the RASSI procedure with a spin-orbit Hamiltonian. The single-ion magnetic properties and LF parameters were calculated on the basis of the ab initio data with the use of a SINGLE ANISO module.^[35]

Phonon spectra modeling and analysis were performed with in-house Python scripts based on ASE libraries and with the improved version of some functions.^[36] The DFTB+ software^[29b] was used as a force derivation code in the Calculator class of ASE. The finite differences method was used in phonon calculations with atomic displacement of 0.03 Å along each Cartesian axis. Prior to phonon calculations, 1D and 3D systems (see Figure S11 in the Supporting Information) were optimized with a quasi-Newton algorithm down to 0.0002 eV Å⁻¹ with 2 k -point sampling in each periodic direction. In all calculations, the non-charge-self-consistent model was employed with the Slater-Koster parameters developed for similar types of system.^[37]

Acknowledgements

The authors acknowledge funding from the European Union's Horizon 2020 research and innovation program, the European Research Council (grant agreement no. 648295 to A.A.P.), a Marie Skłodowska-Curie Action (grant agreement no. 748635 to S.M.A.), and the Deutsche Forschungsgemeinschaft (grants PO 1602/4-1 and PO 1602/5-1 to A.A.P.). R.W. thanks the Swedish Research Council (grant no. 2015-00455) and Marie Skłodowska-Curie Actions co-founding project INCA 600398. T.G. acknowledges support from the Swiss National Science Foundation (Projects No. 206021_150784, and No. 200021L_147201). Computational resources were provided by the Center for High Performance Computing at TU Dresden. We appreciate the technical support with computational resources at IFW Dresden by Ulrike Nitzsche. Sandra Schiemenz is acknowledged for her help with Raman measurements, and Dr. Anja Wolter-Giraud and Sebastian Gaß are acknowledged for their help with magnetic measurements at IFW Dresden.

Conflict of interest

The authors declare no conflict of interest.

Keywords: dysprosium · exchange interactions · fullerenes · lutetium · magnetic properties · phonons

- [1] a) A. A. Popov, S. Yang, L. Dunsch, *Chem. Rev.* **2013**, *113*, 5989–6113; b) S. Yang, T. Wei, F. Jin, *Chem. Soc. Rev.* **2017**, *46*, 5005–5058; c) T. Wang, C. Wang, *Small* **2019**, *15*, 1901522; d) *Endohedral Fullerenes: Electron Transfer and Spin* (Ed.: A. A. Popov), Springer International Publishing, Cham, **2017**.
- [2] a) V. Vieru, L. Ungur, L. F. Chibotaru, *J. Phys. Chem. Lett.* **2013**, *4*, 3565–3569; b) Y. Zhang, D. Krylov, M. Rosenkranz, S. Schiemenz, A. A. Popov, *Chem. Sci.* **2015**, *6*, 2328–2341; c) F. Cimpoesu, N. Dragoe, H. Ramanantoanina, W. Urland, C. Daul, *Phys. Chem. Chem. Phys.* **2014**, *16*, 11337–11348; d) D. S. Krylov, F. Liu, S. M. Avdoshenko, L. Spree, B. Weise, A. Waske, A. U. B. Wolter, B. Büchner, A. A. Popov, *Chem. Commun.* **2017**, 53, 7901–7904; e) W. Yang, G. Velkos, F. Liu, S. M. Sudarkova, Y. Wang, J. Zhuang, H. Zhang, X. Li, X. Zhang, B. Büchner, S. M. Avdoshenko, A. A. Popov, N. Chen, *Adv. Sci.* **2019**, *6*, 1901352; f) C.-H. Chen, D. S. Krylov, S. M. Avdoshenko, F. Liu, L. Spree, R. Yadav, A. Alvertis, L. Hozoi, K. Nenkov, A. Kostanyan, T. Greber, A. U. B. Wolter, A. A. Popov, *Chem. Sci.* **2017**, *8*, 6451–6465; g) M. K. Singh, G. Rajaraman, *Chem. Commun.* **2016**, *52*, 14047–14050.
- [3] a) R. Westerström, J. Dreiser, C. Piamonteze, M. Muntwiler, S. Weyeneth, K. Krämer, S.-X. Liu, S. Decurtins, A. Popov, S. Yang, L. Dunsch, T. Greber, *Phys. Rev. B* **2014**, *89*, 060406; b) A. L. Svitova, Y. Krupskaya, N. Samoylova, R. Kraus, J. Geck, L. Dunsch, A. A. Popov, *Dalton Trans.* **2014**, *43*, 7387–7390; c) C. F. Hermanns, M. Bernien, A. Krüger, C. Schmidt, S. T. Waßerroth, G. Ahmadi, B. W. Heinrich, M. Schneider, P. W. Brouwer, K. J. Franke, E. Weschke, W. Kuch, *Phys. Rev. Lett.* **2013**, *111*, 167203; d) B. Náfrádi, Á. Antal, Á. Pásztor, L. Forró, L. F. Kiss, T. Fehér, É. Kováts, S. Pekker, A. Jánossy, *J. Phys. Chem. Lett.* **2012**, *3*, 3291–3296; e) M. C. Qian, S. V. Ong, S. N. Khanna, M. B. Knickelbein, *Phys. Rev. B* **2007**, *75*, 104424.
- [4] a) D. Gatteschi, R. Sessoli, J. Villain, *Molecular Nanomagnets*, Oxford University Press, New York, **2006**; b) C. Benelli, D. Gatteschi, *Introduction to Molecular Magnetism*, Wiley-VCH, Weinheim, **2015**; c) R. A. Layfield, M. Murugesu, *Lanthanides and Actinides in Molecular Magnetism*, Wiley-VCH, Weinheim, **2015**; d) D. N. Woodruff, R. E. P. Winpenny, R. A. Layfield, *Chem. Rev.* **2013**, *113*, 5110–5148; e) E. Bartolomé, A. Arauzo, J. Luzón, J. Bartolomé, F. Bartolomé in *Handbook of Magnetic Materials*, Vol. 26 (Ed.: E. Brück), Elsevier, Amsterdam, **2017**, pp. 1–289; f) J.-L. Liu, Y.-C. Chen, M.-L. Tong, *Chem. Soc. Rev.* **2018**, *47*, 2431–2453; g) K. L. M. Harriman, D. Errulat, M. Murugesu, *New Trends Chem. Teach.* **2019**, *1*, 425–439; h) P. Zhang, L. Zhang, J. Tang, *Dalton Trans.* **2015**, *44*, 3923–3929; i) J. Dreiser, *J. Phys. Condens. Matter* **2015**, *27*, 183203; j) J. Lu, M. Guo, J. Tang, *Chem. Asian J.* **2017**, *12*, 2772–2779; k) Z. Zhu, M. Guo, X.-L. Li, J. Tang, *Coord. Chem. Rev.* **2019**, *378*, 350–364; l) F. Liu, L. Spree, D. S. Krylov, G. Velkos, S. M. Avdoshenko, A. A. Popov, *Acc. Chem. Res.* **2019**, *52*, 2981–2993.
- [5] a) J. Dreiser, R. Westerström, Y. Zhang, A. A. Popov, L. Dunsch, K. Krämer, S.-X. Liu, S. Decurtins, T. Greber, *Chem. Eur. J.* **2014**, *20*, 13536–13540; b) F. Liu, S. Wang, C.-L. Gao, Q. Deng, X. Zhu, A. Kostanyan, R. Westerström, F. Jin, S.-Y. Xie, A. A. Popov, T. Greber, S. Yang, *Angew. Chem. Int. Ed.* **2017**, *56*, 1830–1834; *Angew. Chem.* **2017**, *129*, 1856–1860; c) F. Liu, C.-L. Gao, Q. Deng, X. Zhu, A. Kostanyan, R. Westerström, S. Wang, Y.-Z. Tan, J. Tao, S.-Y. Xie, A. A. Popov, T. Greber, S. Yang, *J. Am. Chem. Soc.* **2016**, *138*, 14764–14771.
- [6] a) L. Spree, A. A. Popov, *Dalton Trans.* **2019**, *48*, 2861–2871; b) D. Krylov, F. Liu, A. Brandenburg, L. Spree, V. Bon, S. Kaskel, A. Wolter, B. Buchner, S. Avdoshenko, A. A. Popov, *Phys. Chem. Chem. Phys.* **2018**, *20*, 11656–11672; c) A. Brandenburg, D. S. Krylov, A. Beger, A. U. B. Wolter, B. Büchner, A. A. Popov, *Chem. Commun.* **2018**, *54*, 10683–10686; d) R. Westerström, J. Dreiser, C. Piamonteze, M. Muntwiler, S. Weyeneth, H. Brune, S. Rusponi, F. Nolting, A. Popov, S. Yang, L. Dunsch, T. Greber, *J. Am. Chem. Soc.* **2012**, *134*, 9840–9843; e) C. Schliesier, L. Spree, A. Kostanyan, R. Westerström, A. Brandenburg, A. U. B. Wolter, S. Yang, T. Greber, A. A. Popov, *Chem. Commun.* **2018**, *54*, 9730–9733; f) K. Junghans, C. Schliesier, A. Kostanyan, N. A. Samoylova, Q. Deng, M. Rosenkranz, S. Schiemenz, R. Westerström, T. Greber, B. Büchner, A. A. Popov, *Angew. Chem. Int. Ed.* **2015**, *54*, 13411–13415; *Angew. Chem.* **2015**, *127*, 13609–13613.
- [7] a) J. Zhang, S. Stevenson, H. C. Dorn, *Acc. Chem. Res.* **2013**, *46*, 1548–1557; b) M. N. Chaur, F. Melin, A. L. Ortiz, L. Echegoyen, *Angew. Chem. Int. Ed.* **2009**, *48*, 7514–7538; *Angew. Chem.* **2009**, *121*, 7650–7675.
- [8] a) S. F. Yang, S. I. Troyanov, A. A. Popov, M. Krause, L. Dunsch, *J. Am. Chem. Soc.* **2006**, *128*, 16733–16739; b) M. M. Olmstead, T. Zuo, H. C. Dorn, T. Li, A. L. Balch, *Inorg. Chim. Acta* **2017**, *468*, 321–326; c) C. Schliesier, F. Liu, V. Dubrovin, L. Spree, B. Büchner, S. Avdoshenko, A. A. Popov, *Nanoscale* **2019**, *11*, 13139–13153.
- [9] a) A. Kostanyan, R. Westerström, Y. Zhang, D. Kunhardt, R. Stania, B. Büchner, A. A. Popov, T. Greber, *Phys. Rev. Lett.* **2017**, *119*, 237202; b) Y. Zhang, D. Krylov, S. Schiemenz, M. Rosenkranz, R. Westerstrom, J. Dreiser, T. Greber, B. Buchner, A. A. Popov, *Nanoscale* **2014**, *6*, 11431–11438; c) Z. Zhang, Y. Liu, P. Han, S. Zhuang, T. Wang, S. Luo, B. Xu, *ChemPhys-Chem* **2015**, *16*, 295–298; d) M. Nie, J. Xiong, C. Zhao, H. Meng, K. Zhang, Y. Han, J. Li, B. Wang, L. Feng, C. Wang, T. Wang, *Nano Res.* **2019**, *12*, 1727–1731.
- [10] R. Orbach, *Proc. R. Soc. London Ser. A* **1961**, *264*, 458–484.
- [11] a) K. N. Shrivastava, *Phys. Status Solidi B* **1983**, *117*, 437–458; b) A. Singh, K. N. Shrivastava, *Phys. Status Solidi B* **1979**, *95*, 273–277.
- [12] S. T. Liddle, J. van Slageren, *Chem. Soc. Rev.* **2015**, *44*, 6655–6669.
- [13] P. G. Klemens, *Phys. Rev.* **1962**, *125*, 1795–1798.
- [14] a) D. L. Mills, *Phys. Rev.* **1966**, *146*, 336–343; b) M. B. Walker, *Phys. Rev.* **1967**, *162*, 199–208; c) J. G. Castle, D. W. Feldman, *Phys. Rev.* **1965**, *137*, A671–A673.
- [15] K. W. H. Stevens, *Rep. Prog. Phys.* **1967**, *30*, 189–226.
- [16] Y.-S. Ding, K.-X. Yu, D. Reta, F. Ortu, R. E. P. Winpenny, Y.-Z. Zheng, N. F. Chilton, *Nat. Commun.* **2018**, *9*, 3134.
- [17] A. Lunghi, F. Totti, R. Sessoli, S. Sanvito, *Nat. Commun.* **2017**, *8*, 14620.
- [18] M. E. Lines, *J. Chem. Phys.* **1971**, *55*, 2977–2984.
- [19] a) C. A. P. Goodwin, F. Ortu, D. Reta, N. F. Chilton, D. P. Mills, *Nature* **2017**, *548*, 439–442; b) L. Escalera-Moreno, N. Suaud, A. Gaita-Ariño, E. Coronado, *J. Phys. Chem. Lett.* **2017**, *8*, 1695–1700.
- [20] L. Escalera-Moreno, J. J. Baldoví, A. Gaita-Ariño, E. Coronado, *Chem. Sci.* **2018**, *9*, 3265–3275.
- [21] M. Atzori, S. Benci, E. Morra, L. Tesi, M. Chiesa, R. Torre, L. Sorace, R. Sessoli, *Inorg. Chem.* **2018**, *57*, 731–740.
- [22] a) S. F. Yang, A. A. Popov, M. Kalbac, L. Dunsch, *Chem. Eur. J.* **2008**, *14*, 2084–2092; b) A. A. Popov, *J. Comput. Theor. Nanosci.* **2009**, *6*, 292–317.
- [23] a) B. G. Burke, J. Chan, K. A. Williams, J. C. Ge, C. Y. Shu, W. J. Fu, H. C. Dorn, J. G. Kushmerick, A. A. Puzos, D. B. Geohegan, *Phys. Rev. B* **2010**, *81*, 115423; b) M. Krause, X. J. Liu, J. Wong, T. Pichler, M. Knupfer, L. Dunsch, *J. Phys. Chem. A* **2005**, *109*, 7088–7093.
- [24] a) M. Ganzhorn, S. Klyatskaya, M. Ruben, W. Wernsdorfer, *Nat. Commun.* **2016**, *7*, 11443; b) M. Ganzhorn, S. Klyatskaya, M. Ruben, W. Wernsdorfer, *Nat. Nanotechnol.* **2013**, *8*, 165.
- [25] S. Lebedkin, B. Renker, R. Heid, H. Schober, H. Rietschel, *Appl. Phys. A* **1998**, *66*, 273–280.
- [26] a) M. Hulman, M. Krause, H. Kuzmany, M. Inakuma, H. Shinohara, *Ferroelectrics* **2001**, *249*, 107–115; b) S. M. Grannan, J. T. Birmingham, P. L. Richards, D. S. Bethune, M. S. deVries, P. H. M. vanLoosdrecht, H. C. Dorn, P. Burbank, J. Bailey, S. Stevenson, *Chem. Phys. Lett.* **1997**, *264*, 359–365.
- [27] a) L. Pintschovius, *Rep. Prog. Phys.* **1996**, *59*, 473–510; b) S. F. Parker, S. M. Bennington, J. W. Taylor, H. Herman, I. Silverwood, P. Albers, K. Refson, *Phys. Chem. Chem. Phys.* **2011**, *13*, 7789–7804.
- [28] a) R. Bini, P. Procacci, P. R. Salvi, V. Schettino, *J. Phys. Chem.* **1993**, *97*, 10580–10584; b) G. Kato, C. Yokomizo, H. Omata, M. Sato, T. Ishii, K. Nagasaka, *Solid State Commun.* **1995**, *93*, 801–804; c) P. J. Horoyksi, M. L. W. Thewalt, T. R. Anthony, *Phys. Rev. B* **1995**, *52*, R6951–R6954.
- [29] a) D. Porezag, T. Frauenheim, T. Köhler, G. Seifert, R. Kaschner, *Phys. Rev. B* **1995**, *51*, 12947–12957; b) B. Aradi, B. Hourahine, T. Frauenheim, *J. Phys. Chem. A* **2007**, *111*, 5678–5684.
- [30] a) T. Heine, K. Vietze, G. Seifert, *Magn. Reson. Chem.* **2004**, *42*, S199–S201; b) M. Krause, H. Kuzmany, P. Georgi, L. Dunsch, K. Vietze, G. Seifert, *J. Chem. Phys.* **2001**, *115*, 6596–6605.

- [31] N. F. Chilton, R. P. Anderson, L. D. Turner, A. Soncini, K. S. Murray, *J. Comput. Chem.* **2013**, *34*, 1164–1175.
- [32] a) J. Hafner, *J. Comput. Chem.* **2008**, *29*, 2044–2078; b) G. Kresse, J. Hafner, *Phys. Rev. B* **1993**, *47*, 558–561; c) G. Kresse, D. Joubert, *Phys. Rev. B* **1999**, *59*, 1758–1775; d) J. P. Perdew, K. Burke, M. Ernzerhof, *Phys. Rev. Lett.* **1996**, *77*, 3865–3868; e) S. Grimme, *WIREs Comput. Mol. Sci.* **2011**, *1*, 211–228.
- [33] a) B. O. Roos, R. Lindh, P.-Å. Malmqvist, V. Veryazov, P.-O. Widmark, A. C. Borin, *J. Phys. Chem. A* **2008**, *112*, 11431–11435; b) B. O. Roos, R. Lindh, P.-Å. Malmqvist, V. Veryazov, P.-O. Widmark, *J. Phys. Chem. A* **2005**, *109*, 6575–6579; c) B. O. Roos, R. Lindh, P.-Å. Malmqvist, V. Veryazov, P.-O. Widmark, *J. Phys. Chem. A* **2004**, *108*, 2851–2858.
- [34] F. Aquilante, J. Autschbach, R. K. Carlson, L. F. Chibotaru, M. G. Delcey, L. De Vico, I. Fdez. Galván, N. Ferré, L. M. Frutos, L. Gagliardi, M. Garavelli, A. Giussani, C. E. Hoyer, G. Li Manni, H. Lischka, D. Ma, P. Å. Malmqvist, T. Müller, A. Nenov, M. Olivucci, T. B. Pedersen, D. Peng, F. Plasser, B. Pritchard, M. Reiher, I. Rivalta, I. Schapiro, J. Segarra-Martí, M. Stenrup, D. G. Truhlar, L. Ungur, A. Valentini, S. Vancoillie, V. Veryazov, V. P. Vysotskiy, O. Weingart, F. Zapata, R. Lindh, *J. Comput. Chem.* **2016**, *37*, 506–541.
- [35] L. F. Chibotaru, L. Ungur, *J. Chem. Phys.* **2012**, *137*, 064112.
- [36] L. A. Hjorth Larsen, M. J. Jørgen, B. Jakob, E. C. Ivano, C. Rune, D. Marcin, F. Jesper, N. G. Michael, H. Bjørk, H. Cory, D. H. Eric, C. J. Paul, J. P. Bjerre, K. James, R. K. John, K. E. Leonhard, K. Joseph, K. Kristen, L. Steen, M. J. Bergmann, M. Tristan, O. Thomas, P. Lars, P. Andrew, R. Carsten, S. Jakob, S. Ole, S. Mikkel, S. T. Kristian, V. Tejs, V. Lasse, W. Michael, Z. Zhenhua, W. J. Karsten, *J. Phys. Condens. Matter* **2017**, *29*, 273002.
- [37] G. Zheng, H. A. Witek, P. Bobadova-Parvanova, S. Irle, D. G. Musaev, R. Prabhakar, K. Morokuma, M. Lundberg, M. Elstner, C. Köhler, T. Frauenheim, *J. Chem. Theory Comput.* **2007**, *3*, 1349–1367.

Manuscript received: October 25, 2019

Accepted manuscript online: November 27, 2019

Version of record online: February 6, 2020
